Lego-inspired reconfigurable modular blocks for automated construction of engineering structures

Rojyar Barhemat [a], Soroush Mahjoubi [a], Victor C. Li [b], Yi Bao [a],[*]

[a] *Department of Civil, Environmental and Ocean Engineering, Stevens Institute of Technology, Hoboken, NJ 07030, USA*
[b] *Department of Civil and Environmental Engineering, University of Michigan, Ann Arbor, MI 48109, USA*

ARTICLE INFO

ABSTRACT

Reconfigurable modular structures are able to be assembled using prefabricated modules and reconfigured to promote automated construction and to improve sustainability and resilience of infrastructure, while the computer-aided design and modeling of the modules are unclear. This study develops a many-objective optimization approach to design the modules made using strain-hardening cementitious composite. The proposed approach integrates a sequential surrogate model, Latin hypercube sampling method, Unified Non-dominated Sorting Genetic Algorithm III, and Technique for Order of Preference by Similarity to Ideal Solution to predict and optimize the properties of assemblages of the modules. Four objective functions were defined using the load-carrying capacity, deformability, stiffness, and volume. Results showed that the proposed method had reasonable prediction accuracy. The optimal design increased the load-carrying capacity, deformability, and stiffness by 22.8%, 11.5%, and 129.2%, respectively, and reduced the volume by 51.6%. This study is expected to effectively improve the design of reconfigurable modular structures.

1. Introduction

The productivity in the construction industry decreased in the past decade while it rapidly increased in the manufacturing industry [1]. The rapid growth of productivity is associated with adoption of automation techniques in manufacturing. In the era of Industry 4.0 [2], intelligent manufacturing is projected to further improve the productivity. The low productivity of the construction industry is associated with limitations in the construction efficiency, quality, and safety, as well as the lack of skilled labor [3]. Although development of construction equipment improved the construction efficiency, such as the increase of payloads of lifting equipment, the construction methods of infrastructure such as bridges and buildings still employ the methods developed more than a hundred years ago. In summary, advances in automation and machine intelligence are not fully utilized in the construction industry.

Modular construction was proposed to improve the construction efficiency, quality, and safety by taking advantage of off-site prefabrication and on-site assembly [4]. Compared with cast-in-place concrete structures, the prefabrication of structural modules in factories is capable of achieving higher quality and reducing environmental impacts in terms of the material and energy consumption, carbon emission, and

pollution; and the rapid assembly of prefabricated modules reduces the construction time and occurrence of construction incidents. It was reported that the construction time was reduced by 50% compared with the conventional monolithic construction method [3]. The improvement of construction efficiency not only saves costs but also improves the mobility of transportation infrastructure by minimizing the downtime for construction and rehabilitation. Thus, modular construction represents a more sustainable and efficient solution compared with the conventional methods. Besides, modular construction is capable of incorporating applications of construction robots and intelligent technologies such as building information modeling and sensing technologies [5], thus significantly improving the construction efficiency and precision while alleviating intervention of human. The adoption of automation in construction further reduces the incidents and quality issues associated with human misconducts. Because of the many advantages, modular construction was applied to different types of structures, such as buildings and bridges [6–9]. For example, modular buildings were built by stacking prefabricated modular rooms [6,7]; and modular bridges were built by assembling prefabricated bridge components such as girders and slabs [8,9]. The prefabricated building and bridge components were assembled at joints that were designed to

* Corresponding author.
  E-mail address: yi.bao@stevens.edu (Y. Bao).

provide sufficient load-carrying capacity for the connected components [10,11].

Despite the many advantages, existing modular construction paradigm does not allow the reuse of structural modules. The end-of-life management of the structural modules mainly involves landfill, which involves additional expenses, carbon emission, and pollution [12]. Although it is possible to recycle structural materials such as steel and concrete, the recycling process is complex and involves significant costs, carbon emission, and energy consumption [13]. Also, it should be noted that the recycled materials often have lower mechanical property and durability. For example, recycled concrete aggregate was produced by sorting, crushing, and cleaning waste concrete, and used to produce recycled concrete, but the use of recycled concrete aggregates reduced the compressive strength and durability of concrete [14,15].

Recently, reconfigurable modular structures inspired by Lego toys were proposed as a new concept of modular structures [16]. Reconfigurable modular structures were assembled using structural modules, and they could be disassembled and reconfigured for different structures. For example, a modular footbridge was disassembled, as shown in. Fig. 1, and the footbridge was disassembled to reuse the modules to assemble a beam-column frame for buildings [16]. Experiments were conducted to demonstrate the load-carrying capability and reconfigurability of the footbridge. The concept of reconfigurable modular structures showed major advantages. On one hand, the reusability of reconfigurable modular structures creates a new avenue to improve the sustainability because reuse of structural modules does not involve the complex processes and performance degradation of recycling of structural modules. Damaged modules can be replaced by intact modules while retaining the other modules, and the damaged modules can be recycled to produce new modules.

On the other hand, the reconfigurability is expected to improve resilience of structures to extreme events such as earthquake and fire because damaged structures can be rapidly strengthened or repaired by replacing damaged modules. In a nutshell, the concept of reconfigurable modular structures is promising to improve the sustainability and resilience of structures. Following the concept of reconfigurable modular structures, a set of four types of modular blocks were proposed, as depicted in Fig. 1, in the feasibility study reported in reference [16]. The modular blocks were used to assemble the footbridge, and they were connected through steel bolts and nuts as well as the shear keys. Currently, there is lack of knowledge about the computer-aided design and modeling of the modular blocks. It is unclear how the blocks should be designed and optimized to achieve high load-carrying capacity,

deformability, and stiffness while minimizing the mass. In addition, the fundamental mechanical behavior of modular blocks is unclear.

To fill these gaps, this study develops a many-objective optimization method to optimize the design of Lego-inspired modular blocks for reconfigurable structures. The main objectives and technical contributions are: (1) to develop a new many-objective optimization framework by integrating sequential surrogate model, Latin hypercube sampling (LHS) method, Unified Non-dominated Sorting Genetic Algorithm III (UNSGA-III), and Technique for Order of Preference by Similarity to Ideal Solution (TOPSIS); and (2) to implement the new framework to obtain the optimal design of the modular blocks for the maximal load-carrying capacity, stiffness, and deflection and the minimal material consumption.

The remainder of the paper is organized as follows: Section 2 introduces the new many-objective optimization method. Section 3 presents the implementation of the many-objective optimization method to design of Lego-inspired blocks. Section 4 summarizes the new findings from this research.

2. Methodology

The methodology is elaborated in five subsections. Section 2.1 gives an overview of the framework. Section 2.2 presents the LHS method used to establish datasets. Section 2.3 elaborates the sequential surrogate modeling method used to generate predictive models. Section 2.4 introduces the UNSGA-III method for optimizing the mechanical properties of assemblages of modular blocks. Section 2.5 presents the TOPSIS method applied to select the optimal design.

2.1. Overview of the framework

Fig. 2 shows the flowchart of the proposed framework for many-objective optimization. The proposed framework includes five main steps: (1) Step 1: A high-fidelity finite element model is developed to predict the mechanical properties of the structures assembled using modular blocks. (2) Step 2: A dataset is generated using the finite element model based on the LHS method [17]. (3) Step 3: Sequential surrogate models are developed using the dataset to replace the finite element model for predicting the mechanical properties. (4) Step 4: The sequential surrogate models [18] are integrated with the UNSGA-III method [19] to perform many-objective optimization for the design of the modular blocks. (5) Step 5: The TOPSIS method [20] is used to determine the optimal design of modular structures.
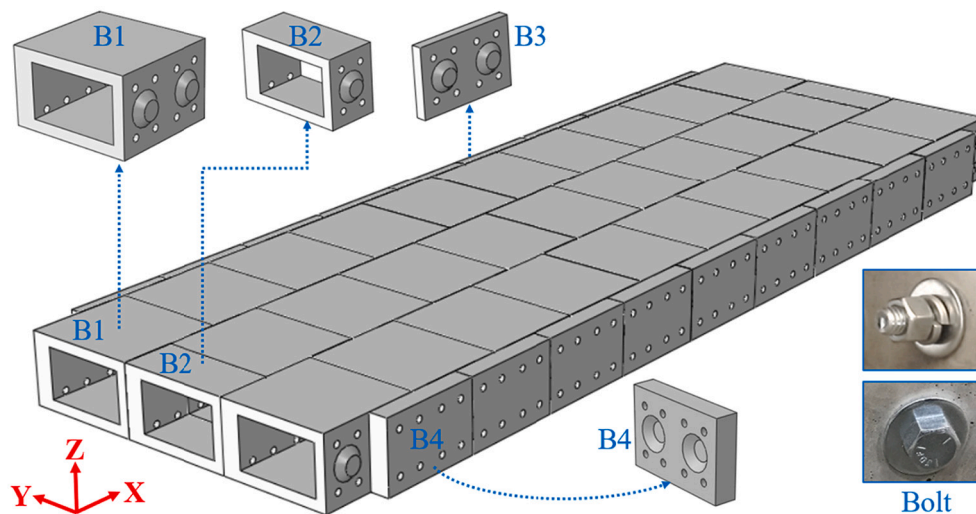

Fig. 1. Illustration of the modular footbridge assembled using four types of modular blocks [16]. B1 to B4 denote the whole block, half block, side plate with male shear keys, and side plate with female shear keys, respectively. Permission was granted for reprint of this figure.
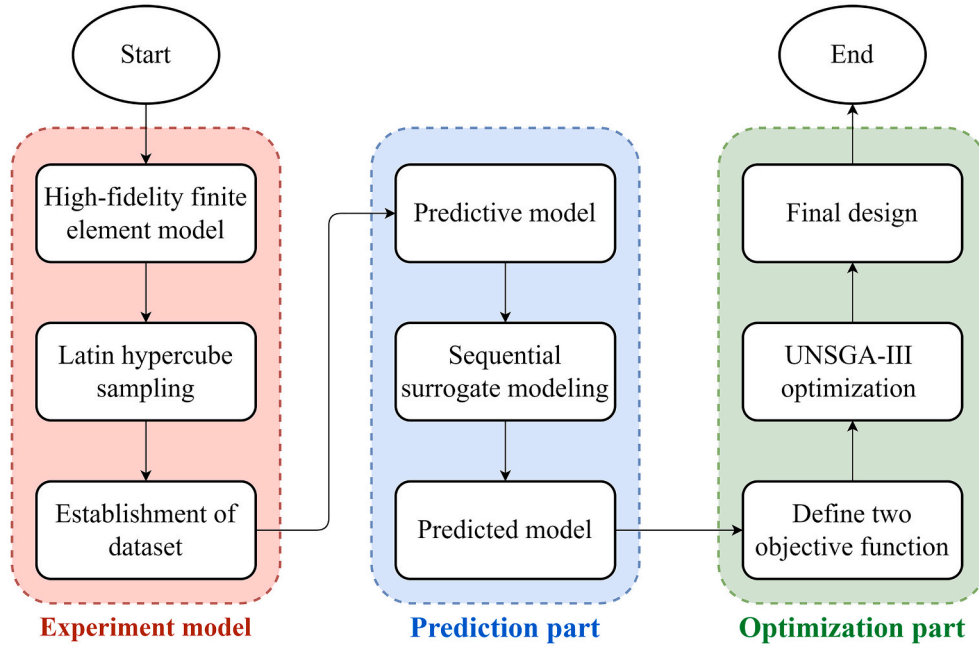
Fig. 2. Depiction of the flowchart of the prediction-optimization framework in this research.

2.2. Establishment of dataset

A dataset was established using high-fidelity finite element models to relate the design variables such as the geometrical dimensions of modules to the mechanical properties of assemblages using the modules. The design variables and mechanical properties are the input and output variables, respectively, used to develop surrogate predictive models. The LHS method, which is a statistical method that selects random samples over the sample space, was adopted to sample the input variables in this study [17]. With the sampled input variables, the output variables were obtained from the high-fidelity finite element models. Previous studies showed that the use of the LHS method effectively reduced the number of finite element models [21]. The LHS method was adopted to acquire representative initial samples among numerous possible combinations of samples. The number of initial samples was set to ten times the number of parameters, as recommended by reference [22]. The established dataset was divided into two sub-sets, which were used to train and validate the surrogate models, respectively.

2.3. Sequential surrogate models

Surrogate modeling is a type of supervised machine learning method that can replace complicated computer simulations such as finite element analysis to improve computational efficiency for prediction of key properties [23,24]. The basic idea of surrogate modeling is to substitute a computationally expensive model with an efficient data-driven model that is sufficiently accurate. Surrogate models can be established using different machine learning methods such as radial basis function model [25], kriging model [26], and artificial neural network [27]. In conventional surrogate modeling, the samples are added by trial and error because the response surface is unknown in advance. The samples spread out uniformly across the parameter space, compromising the efficiency and accuracy, when the response surface is complex and has local variations.

This study adopted a sequential surrogate method with sequential sampling for active learning and property prediction [18]. The training dataset was determined in the training process by sequentially adding samples to the training dataset. The prediction uncertainty was statistically interpreted, and infill criteria were used to update the model by

adding new samples, as illustrated in Fig. 3. The infill criteria were defined using expected improvement and mean square error, which selected samples to enrich the training dataset and improve the model effectively and efficiently.

Fig. 4 shows the flowchart of the sequential surrogate modeling method in seven steps: (1) Step 1: The training and validation datasets are established, as elaborated in Section 2.2. (2) Step 2: A kriging model is trained using the training dataset to predict the mechanical properties of assemblages, as elaborated in Section 2.3.1. (3) Step 3: The trained kriging model is used to predict validation dataset which is unseen to predictive model. (4) Step 4: Two performance metrics, the coefficient of determination (R^2) and root mean square error ($RMSE$), are used to evaluate the accuracy of the kriging model, as elaborated in Section 2.3.2. (5) Step 5: Two stopping criteria are defined to terminate the training process, as elaborated in Section 2.3.3. (6) Step 6: Two infill criteria, the expected improvement and mean square error techniques, are used to add samples to the training dataset to improve the predictive model, as elaborated in Section 2.3.3. (7) Step 7: Steps 3 to 6 are iterated until the stopping criteria are satisfied.

2.3.1. Kriging models

A kriging model [28,29] describes the relationship between the input and output variables. The spatial correlation between the unknown and known variables was used to estimate an unknown function value from the known function values. The correlation matrix between design variables is defined in Eq. (1):

$$T\left(x_i, x_j\right) = exp\left(- \sum_{p=1}^{k} \theta_p \left|\left|x_i^p - x_j^p\right|\right|^2 \right) = corr\left(x_i, x_j\right) \tag{1}$$

where T is the correlation matrix between two input variables x_i and x_j; and θ_p is a vector to scale the correlation length in each dimension. θ_p is obtained by maximizing log-likelihood function, as defined in Eq. (2):

$$L = -\frac{n}{2}ln\left(\sigma^2\right) - \frac{1}{2}ln|T| - \frac{1}{2\sigma^2}(Y - 1\mu)^T T^{-1}(Y - 1\mu) \tag{2}$$

where L is the log-likelihood function of kriging model; n is the number of samples; μ is the mean predicting response; σ^2 is the variance that shows the dispersion of the mean of kriging model; and Y is the values of
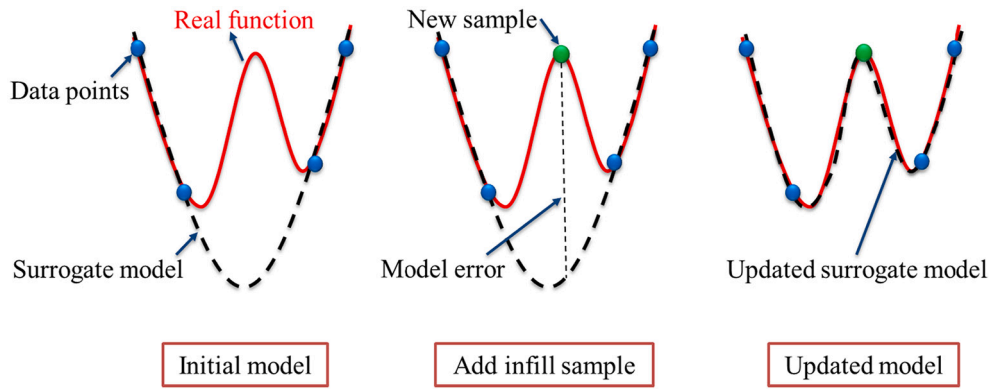
Fig. 3. Illustration of the concept of sequential sampling in sequential surrogate modeling.
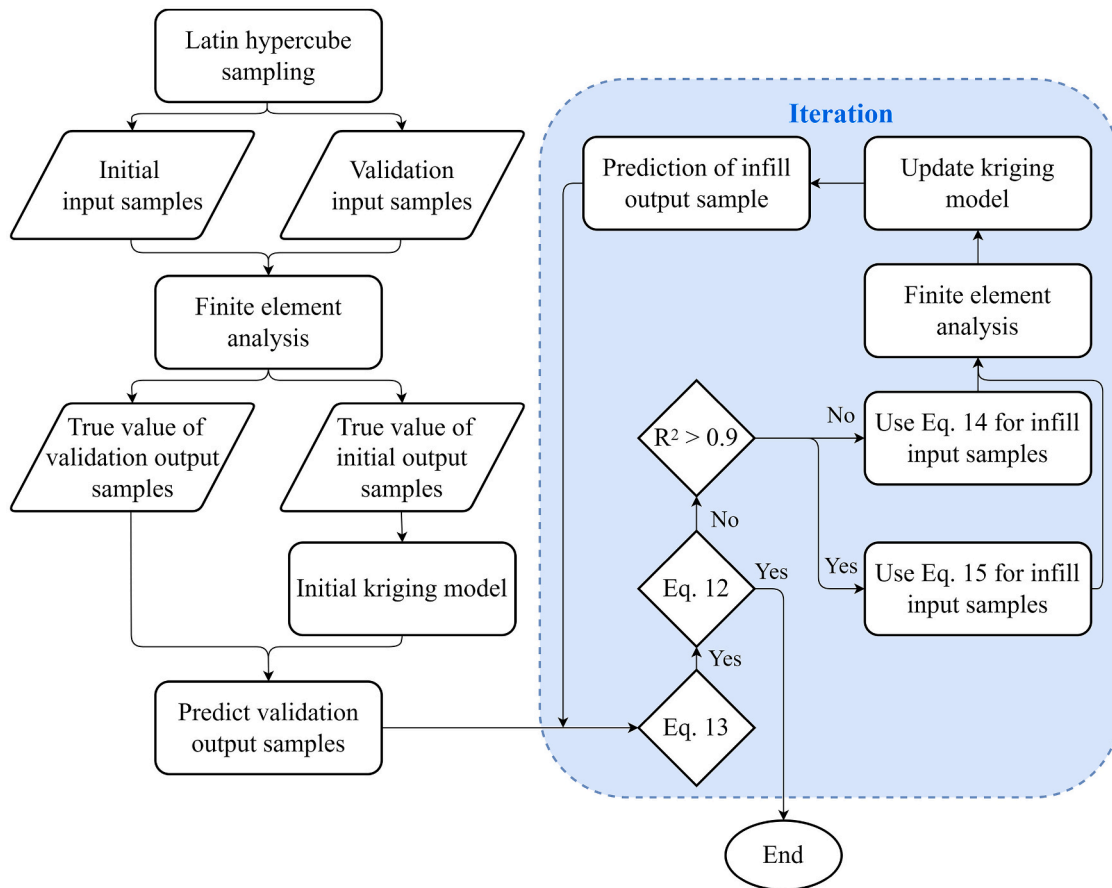

Fig. 4. Flowchart of the procedure of the adopted sequential surrogate modeling method.

a function with *n* samples as shown in Eq. (3):

$$Y = \left[y(x^1), y(x^2), ..., y(x^n) \right]^T \tag{3}$$

When *L* is maximized, μ and σ^2 are obtained as:

$$\sigma^2 = \frac{(Y - 1\mu)^T C^{-1} (Y - 1\mu)}{n} \tag{4}$$

$$\mu = \frac{1^T C^{-1} Y}{1^T C^{-1} 1} \tag{5}$$

where *C* is non-zero covariance function between two samples as shown in Eq. (6):

$$C(x_i, x_j) = \sigma^2 T(x_i, x_j) \tag{6}$$

When μ and σ^2 are obtained, the prediction of new samples of kriging model can determined by Eq. (7).

$$\widehat{y}(x^*) = \mu + t^T T^{-1} (Y - 1\mu) \tag{7}$$

The symbol *t* is the correlation between a new sample (*x**) and the training sample:

$$t(i) = corr(x^*, x_i) \tag{8}$$

2.3.2. Prediction accuracy

Coefficient of determination (R^2) and root mean square error (*RMSE*)

4

are used to evaluate the accuracy of the predictive model, as defined in Eqs. (9) and (10), respectively.

$$R^2(X,Y) = 1 - \frac{\sum\limits_{i=1}^{n}(x_i - y_i)^2}{\sum\limits_{i=1}^{n}[y_i - \text{mean}(y_i)]^2} \tag{9}$$

$$\text{RMSE}(X,Y) = \sqrt{\frac{\sum\limits_{i=1}^{n}(x_i - y_i)^2}{n}} \tag{10}$$

where $X = \{x_1, x_2, ..., x_n\}$ is predicted values; $Y = \{y_1, y_2, ..., y_n\}$ is the actual values; and n is the number of observed data points.

2.3.3. Stopping and infill criteria

After determination the performance metrics of the predictive model, stopping criteria should be inquired to determine whether to stop the training process. Two stopping criteria are used as follows:

$$R_i^2 \geq R_{Thresh}^2 \tag{11}$$

$$|RMSE_i - RMSE_{i+1}| \leq \Delta RMSE_{Thresh}(1 + |RMSE_i|) \tag{12}$$

where subscript i is the number of infill samples; subscript *Thresh* is the threshold of the stopping criteria. For the load capacity, deflection corresponding to the peak load, and stiffness, R_{Thresh}^2 was 0.94, and $\Delta RMSE_{Thresh}$ was 1, 0.2, and 6, respectively.

If the stopping criteria are not satisfied in the training process, new samples should be added to the training dataset to improve the accuracy. Two infill criteria were defined. If R^2 was less than 0.9, Eq. (13) was used to add new samples; otherwise, the expected improvement (EI) is utilized as defined in Eq. (14).

$$\widehat{S}^2(y(x^*)) = \sigma^2(1 - t^T T^{-1} t) \tag{13}$$

$$EI(x) = \frac{y_{min} - \widehat{y}(x^*)}{2}\left[1 + erf\left(\frac{y_{min} - \widehat{y}(x^*)}{\sqrt{2}\,\widehat{S}^2[y(x^*)]}\right)\right] + \frac{\widehat{S}^2[y(x^*)]}{\sqrt{2\pi}} exp\left[\frac{\widehat{y}(x^*) - y_{min}}{2\widehat{S}^2[y(x^*)]}\right] \tag{14}$$

where y_{min} is the current best value; *erf* is the error function; $\widehat{y}(x^*)$ is the prediction of the new sample; $\widehat{y}(x^*)$ and $\widehat{S}^2(y(x^*))$ are the mean and the variance of the random Gaussian process, respectively.

2.4. Optimization algorithms

UNSGA-III [19] and AGE-MOEA [30] algorithms were utilized to perform many-objective optimization, respectively. Hypervolume is a performance indicator to assess the performance of algorithms, as indicated in Fig. 5. Hypervolume is the volume of optimal solutions in the objective space in terms of a reference point. The reference point is the adverse values of the objective function in a dataset. A better solution is determined by a higher hypervolume indicator. The results of the hypervolume indicator for UNSGA-III and AGE-MOEA algorithms are elaborated in Section 3.6.

In many-objective optimization problems, there is no single solution that achieves the optimal results for all objectives. A set of optimal solutions called Pareto optimal solutions are generated by the UNSGA-III. For each Pareto optimal solution, none of the objective functions can be improved without compromising another objective function [19]. The number of generations and population size are set to 300 and 100, respectively. The design constraint is imposed using the mass or volume. The mass of the blocks is limited to 61.2 kg to satisfy the payloads of robots such as MULE ML135 robots [31]. Considering the density of the material, the volume of a block should be less than 27.3 L. The penalty function approach is utilized to apply the mentioned design constraint.
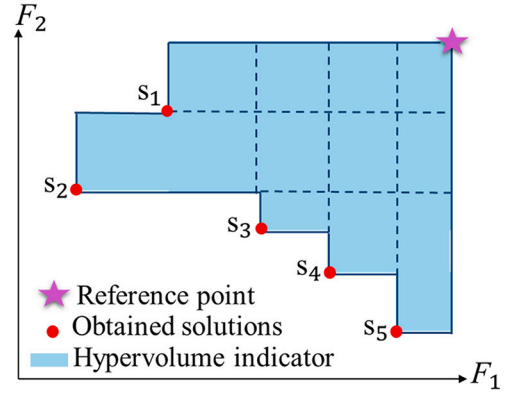

Fig. 5. Hypervolume indicator of a bi-objective optimization problem; F_1 and F_2 are the two objective functions.

The penalty function converts the constrained optimization problem into an unconstrained one. The objective function is redefined as follows:

$$F_{Penalty} = F \times f_{penalty} \tag{15}$$

Penalized objective function is shown with $F_{Penalty}$, and $f_{penalty}$ is the penalty function, which is defined as:

$$f_{penalty} = (1 + \varepsilon_1 \times \gamma)^{\varepsilon_2} \tag{16}$$

where γ is the violation of the design limits, which can be calculated as:

$$\gamma = \sum_{i=1}^{n} V_i, \tag{17}$$

$$V_i = 1 - \frac{F_{max}}{F} \text{ if } F > F_{max} \text{ otherwise } V = 0 \tag{18}$$

The parameters ε_1 and ε_2 are two constant parameters. ε_1 is set to 1, while ε_2 linearly increases from 1.3 to 3 during the optimization process, according to reference [32].

2.5. Selection of optimal solutions

Since UNSGA-III does not have a single optimal solution, the Technique for Order of Preference by Similarity to Ideal Solution (TOPSIS) is used to determine an optimal solution. TOPSIS is a method for the determining many-objective optimization by sorting the Pareto optimal solutions obtained from UNSGA-III [20]. The basic mechanism of TOPSIS is to calculate the distance between each solution and the ideal solution, as well as the distance between each solution and the worst solution, in a k-dimensional objective space with k objective functions. The solution with the highest rank is the closest to the ideal solution and the furthest away from the worst solution. To rank m number of Pareto optimal solutions of a many-objective problem with k number of objective functions, TOPSIS uses the following procedure:

- Eq. (19) determines the ideal and worst solutions:

$$\text{R}^+ = \left\{\left(Min(\rho_{i,j}) \mid i = 1,2,...,m \mid j \in J^-\right), \left(Max(\rho_{i,j}) \mid i = 1,2,...,m \mid j \in J^+\right)\right\}$$
$$= \left\{\text{R}_1^+, \text{Rs}_2^+, ..., \text{R}_k^+\right\} \tag{19a}$$

$$\text{R}^- = \left\{\left(Max(\rho_{i,j}) \mid i = 1,2,...,m \mid j \in J^-\right), \left(Min(\rho_{i,j}) \mid i = 1,2,...,m \mid j \in J^+\right)\right\}$$
$$= \left\{\text{R}_1^-, \text{R}_2^-, ..., \text{R}_k^-\right\} \tag{19b}$$

where the ideal and worst solutions are R^+ and R^-; k and m are the number of objective functions and solutions; The objective functions to

be maximized and minimized are denoted by J^+, J^-; and $\rho_{i,j}$ is the normalized objective function that can obtain as follows:

- Eq. (20) normalizes the objective function values of the Pareto optimal solutions:

$$\rho_{i,j} = \frac{A_{i,j}}{\sqrt{\sum_{k=1}^{m} A_{k,j}^2}} \tag{20}$$

where subscripts i and j refer to the i-th Pareto optimal solution and j-th objective function value, respectively; and $A_{i,j}$ is the actual value of objective function.

- The distance between the Pareto optimal and ideal and worst solutions is determined as:

$$d_{i,I} = \sqrt{\sum_{j=1}^{m} \left(\rho_{i,j} - R_j^+ \right)^2} \tag{21a}$$

$$d_{i,W} = \sqrt{\sum_{j=1}^{m} \left(\rho_{i,j} - R_j^- \right)^2} \tag{21b}$$

where subscripts i, I, and W are the i-th Pareto optimal solution, ideal solutions, and worst solutions, respectively. Therefore, $d_{i,I}$ and $d_{i,W}$ are the distances between Pareto optimal solution to the ideal and the worst solutions, respectively; and R_j^+ and R_j^- are the j-th components of the ideal and the worst solutions, respectively.

- Each of the Pareto optimal solutions' similarity score can be calculated as:

$$\tau = \frac{d_{i,W}}{d_{i,I} + d_{i,W}} \tag{22}$$

- The similarity score is used to rank the Pareto optimal solutions. The Pareto optimal solution with the highest similarity score comes in first and is chosen as the final solution.

3. Optimization of modular blocks

3.1. Initial design

The preliminary design of a set of four types of blocks was selected as the initial design for the optimization process. The initial design considered the manufacturing, assembling, and disassembling of blocks, as shown in Fig. 6. Each block has four joints at two sides: one side with two male shear keys and the other side with two female shear keys. Each shear key is a circular truncated cone, which measures 20 mm in depth and has two circular sections measuring 90 mm and 50 mm in diameter, respectively. Each shear key is accompanied with four bolt holes, each

hole measuring 20 mm in diameter. The detailed design of the joints is determined to ensure the joints do not fail prior to the block. The performance of the joints was further tested through experiments, as elaborated in Section 3.2. With the designed blocks, a footbridge was assembled to prove the concept, as depicted in Fig. 1.

Based on the initial design, six design variables are considered: the height (H), width 1 (W_1), width 2 (W_2), thickness 1 (T_1), thickness 2 (T_2), and thickness 3 (T_3), as shown in Fig. 7. The range of design variables are determined based on the ranges of validation dataset investigated in Section 3.4, as shown in Table 1.

The modular blocks were made using a type of bendable concrete, which was a version of engineered cementitious composite (ECC) [33–35]. Compared with conventional concrete, ECC features strain-hardening behaviors and high tensile ductility. The tensile stress continues increasing with the increase of tensile strain after the matrix cracks [36]. The unique tension resistance of ECC makes it an appealing structural material for resistance to seismic loading [37–39], impact loading [40], bolting or anchoring force [41], and fire [42]. In addition to the unique tension resistance, ECC has unique crack patterns and durability. Due to the bridging effect of chopped fibers dispersed in ECC matrix, ECC has tight crack widths (less than 60 μm). The controlled crack width ensures that cracked ECC behaves similar to uncracked ECC [43]. Moreover, the tight crack can be self-healed in air with presence of moisture [44]. The healed ECC demonstrated comparable stiffness and permeability with those of intact ECC specimens. The use of PVA fibers in ECC also improved the spalling resistance of ECC at high temperatures [45]. Recently, multifunctionality was imparted into ECC by incorporating functional materials. For instance, titanium dioxide nanoparticles were added to ECC to achieve self-cleaning and air-purifying functions [46].

This study adopted an ECC mixture developed in previous studies [47]. The ingredients of the ECC mixture included Type I Portland
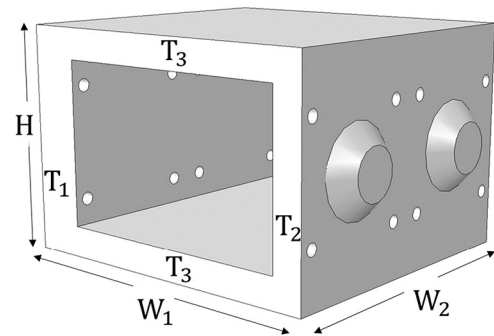
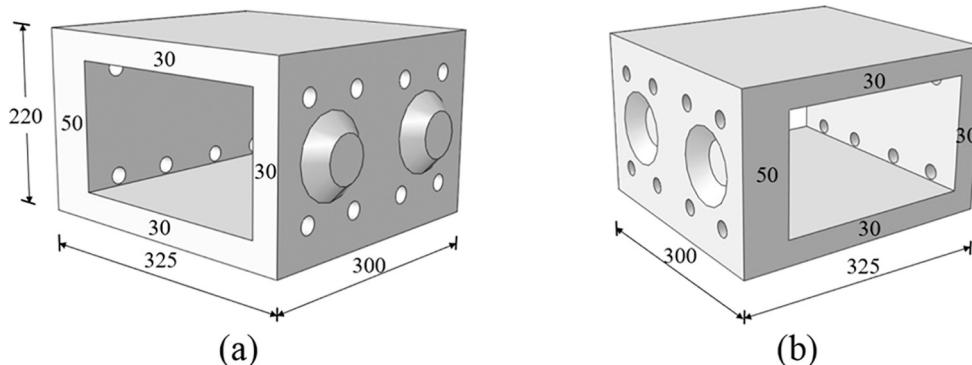**Fig. 7.** Illustration of the variables considered in the optimization of the modular blocks.

Fig. 6. Illustration of a whole block (unit: mm): (a) iso view showing male shear keys, and (b) iso view showing female shear keys.

Table 1
Summary of design variables (mm).

Number	Design variables	Range
1	H	200–400
2	W_1	160–500
3	W_2	200–450
4	T_1	18–75
5	T_2	18–50
6	T_3	18–60

cement, Class F fly ash, silica sand, polyvinyl alcohol (PVA) fibers, water, and chemical admixture. Table 2 lists the chemical and physical properties of the cement and fly ash. The silica sand had a mean diameter (d_{50}) of 75 μm, and its density was 2630 kg/m^3. Table 3 shows the properties of the PVA fibers.

Table 4 lists the ECC mixture. The water-to-binder ratio was 0.25. The sand-to-binder ratio was 0.36. The PVA fiber content was 2% by volume of the mixture. The high-range water reducer (HRWR) was used to achieve adequate flowability of the mixtures.

The mixture was mixed using a 57-L Hobart mixer. First, the dry ingredients cement, fly ash, and quartz sand were added to the mixer and mixed at 60 rpm for 10 min. Then, the HRWR was dissolved in the water and mixed in the mixer at 120 rpm for 6 min. At last, the PVA fibers were added to the mixer. The mixture was mixed at 60 rpm for 3 min, and then, mixed at 120 rpm for 2 min. After the mixing, the mixture was checked, and no agglomeration of the PVA fibers was found, revealing that the PVA fibers were adequately dispersed.

The fresh mixture was used to cast specimens in molds. The specimens were covered with plastic sheets for 24 h and then demolded. After the specimens were demolded, they were cured in air at relative humidity 55% ± 5% and 20 °C ± 2 °C until testing at 28 days. The compressive strengths of the mixture were evaluated using cubic specimens (50 mm × 50 mm × 50 mm) as recommended by ASTM 109C [48] with a loading machine (model: FORNEY F50) at the constant loading rate 0.14 MPa/s. Three samples were replicated in each test. The compressive strength was 61 MPa ± 3 MPa at 28 days.

The tensile properties determined by testing dog-bone specimens, as recommended by the JSCE [49]. Uniaxial tensile test was conducted under displacement control at a displacement rate of 0.5 mm/min. Two external linear variable displacement transducers (LVDTs) were used to measure the elongation of the specimen; the results from the two LVDTs were averaged. As a typical behavior of ECC, closely spaced multiple cracks were generated during the tensile test. Four dog-bone specimens were tested under tension at a displacement rate of 0.05 mm/min in accordance with [46]. The applied load and specimen elongation within the 80-mm gauge length were measured using an embedded load cell and two external linear variable differential transformers, respectively. Fig. 8 shows a set of tensile stress-strain curves. The mixtures had a tensile strength of 5.8 MPa ± 0.2 MPa and an ultimate strain of 4.6% ± 0.3%.

Table 2
Chemical composition and physical properties of cement and fly ash.

Composition or property	Type I Portland cement	Fly ash
SiO_2 (%)	19.51	46.09
Al_2O_3 (%)	3.19	23.15
Fe_2O_3 (%)	2.93	19.48
CaO (%)	63.50	5.08
MgO (%)	2.90	0.77
SO_3 (%)	4.23	1.12
Na_2O (%)	0.07	0.58
K_2O (%)	0.76	1.73
Loss of ignition (%)	2.60	1.99
Density (g/cm^3)	3.15	2.58

Table 3
Properties of the PVA fibers.

Length (mm)	Diameter (mm)	Density (kg/m^3)	Tensile strength (MPa)	Young's modulus (GPa)	Elongation
8	39	1300	1600	43	6%–8%

Table 4
Mixture proportion (kg/m^3).

Cement	Fly ash	Silica sand	Water	HRWR	PVA fibers
400	880	465	320	5.6	26

3.2. Experimental testing

3.2.1. Specimens, test set-up, and instrumentation

The footbridge (Fig. 1) indicates that the connection of blocks is anisotropic and subjected to bending and shear effects. Two types of unit assemblages were designed to evaluate the mechanical responses of assembled structures, as shown in Fig. 9. Specimen 1 had two B1 blocks, one B3 block, and one B4 block, and was tested under three-point bending. Specimen 2 had one B1 block, one B3 block, and one B4 block, and was tested with a double-shear set-up. The specimens were assembled using steel bolts measuring 12.7 mm in diameter and 114.3 mm in length. Steel washers measuring 2 mm in thickness were put in between the bolt/nut and the specimen to distribute the bolting force. The bolt, nut, and washer were made of Grade 8 steel. The Young's modulus of the steel was 210 GPa; the tensile strength was 1034 MPa; and the Poisson's ratio was 0.3. The initial torque applied to tighten the bolt and nut was 50 N·m.

A load frame was used to load the specimens, as shown in Fig. 10. The load frame had an embedded load cell (load capacity: 450 kN) and displacement transducer. A rigid spreader attached to the load frame was used to apply loading. Each specimen was supported on two steel bars that measured 38 mm by 38 mm in the cross section and 305 mm in length. For the flexural test, a third square bar with the same dimensions was placed between the spreader and the specimen at the mid-span. For the shear test, two square bars with the same dimensions were placed between the spreader and the specimen at the mid-span. Each specimen was loaded under displacement control at a displacement rate of 1 mm/min. An optical tracking system (model: NDI Optotrak Certus® HD) was used to measure the deformations. Three-dimensional displacements were measured by the tracker sensors with a manufacturer-specified resolution of 10 μm and a sampling frequency of 4.6 Hz. Specimen 1 was instrumented with ten tracker sensors. Specimen 2 was instrumented with eight tracker sensors.

3.2.2. Failure modes

Fig. 11(a) shows the failure pattern of the assemblage under flexural loading. The first crack appeared at the web of the plate at the mid-span. As the displacement increased, multiple cracks were generated in the side plates that connected the two blocks. The width of the cracks was in the range of 50 μm to 100 μm. The specimen failed until major cracks appeared and propagated successively in the plates. At the top surface of the specimen, minor local crushing was observed at the exterior edge of the contact surface of the two blocks. Fig. 11(c) shows the failure pattern of the assemblage under shear loading. At the early stage of testing, sound of slipping between contacting surfaces was continuously heard, indicating slippage of the plates due to the small gap (1 mm) at the shear keys. The gap was designed to facilitate the assembly of blocks. The first crack appeared at the web plates. As the displacement increased, multiple cracks were generated in the plates that connected the blocks. The damage development process showed that the specimen had good ductility.
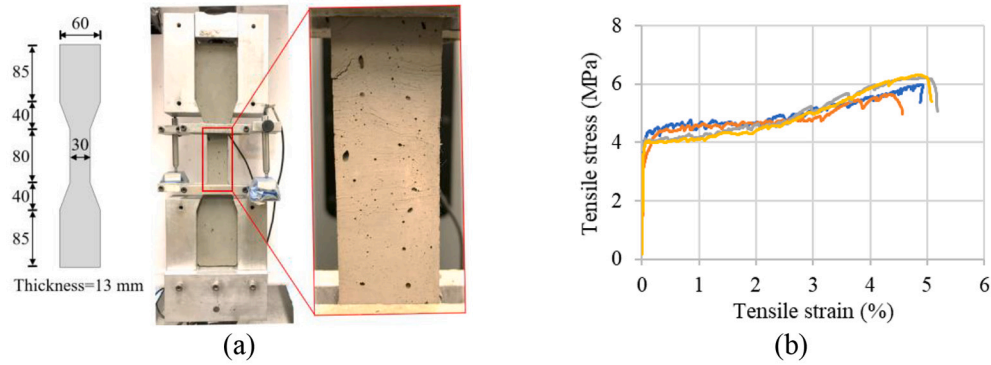
Fig. 8. Tensile test: (a) setup and specimen (unit: mm) [16]; and (b) test result of four specimens. (a) was reprinted with permission.
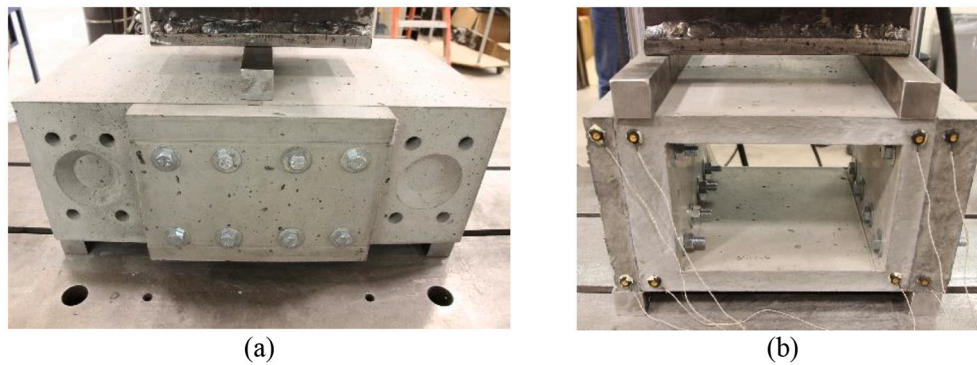

Fig. 9. Mechanical test set-up for the two assemblages: (a) Specimen 1; and (b) Specimen 2.
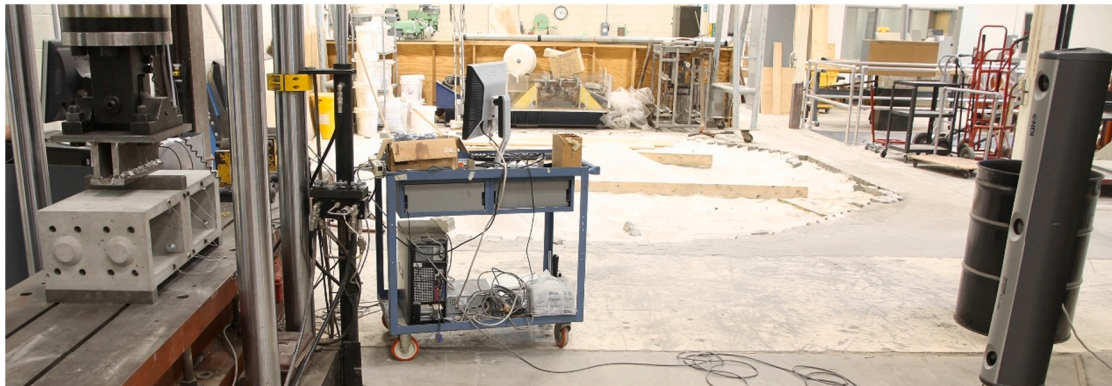

Fig. 10. A camera tracker system used to measure the deformation of blocks in the testing.

3.2.3. Load-displacement relationship

Fig. 12 shows the load-displacement relationships of the bending and shear test specimens. The load linearly increased with the displacement until the first crack occurred. Then, the load increased with a decreasing rate (slope) until the peak load. Finally, the load decreased to zero. The load capacity of specimen 1 is lower than that of specimen 2, revealing that the flexural failure occurs first when the footbridge (Fig. 1) is subjected to increasing loads, so the flexural properties evaluated by specimen 1 controlled the failure of structures assembled by the blocks. Three flexural properties were considered in optimization: (1) the peak load (P_u), characterizing the load capacity; (2) the slope in the linear stage, characterizing the flexural stiffness; and (3) the deflection (D_u) at the peak load, characterizing the ductility and toughness.

3.3. Finite element model

The mechanical behaviors of specimen 1 were simulated using three-dimensional finite element models. The mesh size was 2.5 mm. The ECC of the assemblage was modeled using eight-node solid elements (C3D8R). Surface-to-surface hard contact was used for contact between blocks. Concrete damage plasticity (CDP) was used for modeling the behavior of concrete. Table 5 shows the parameters of concrete damage plasticity.

Fig. 11 compares the failure patterns shown in the experiments and finite element models. The tensile damage index (DAMAGET) is used to show the cracks in the finite element models. A tensile damage index of one indicates complete damage, and a tensile damage index of zero means no crack. The finite element models show consistent crack patterns with the experiments. Fig. 12 compares the load-displacement
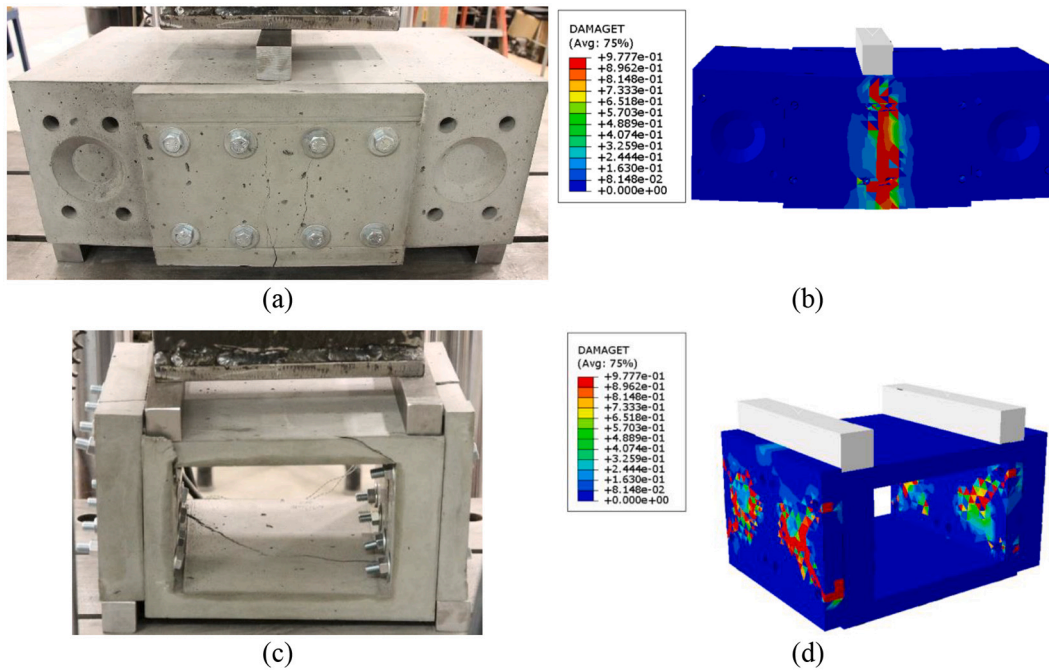
Fig. 11. Failure patterns: (a) assemblage under bending; (b) simulation of assemblage under bending; (c) assemblage under shear force; and (d) simulation of assemblage under shear force.
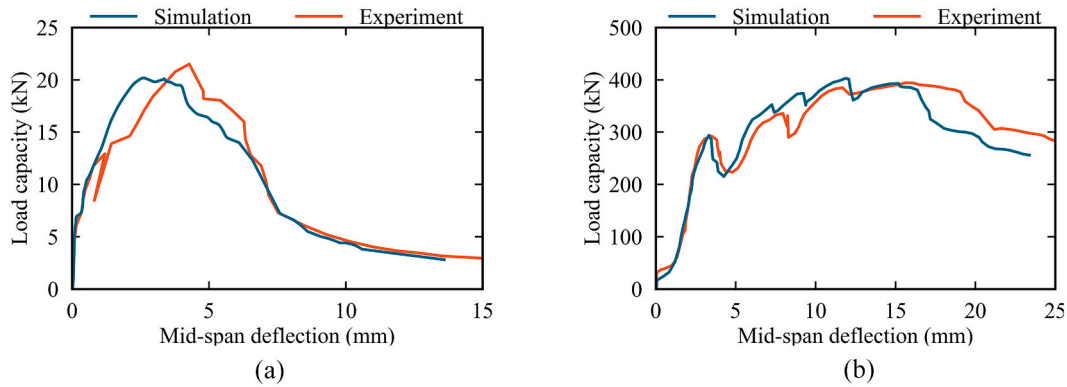

Fig. 12. Load-displacement relationships of specimens under: (a) bending; and (b) shear loads.

Table 5
Parameters of the adopted CDP model.

Density (kg/mm³)	Poisson's ratio	Young's modulus (GPa)	Dilation angle	Eccentricity	fb_0/fc_0	K	Viscosity parameter
2200	0.2	30	36	0.1	1.16	0.67	0

relationships from the finite element model and experiments. The finite element modes are capable of simulating the load-displacement behaviors of the assemblages. In Fig. 12(a), the load capacity results from the finite element model and experiment are 20.2 kN and 21.5 kN, respectively. The finite element model provided reasonable prediction of the mechanical behaviors of the assemblages.

3.4. Parametric analysis results

The finite element model was used to evaluate the effects of design variables H, W_1, W_2, T_1, T_2, and T_3 on the load capacity and ultimate deflection (Fig. A1 in Appendix). A regression analysis was performed to determine the formulae used to describe the effects of the design

variables. As the six design variables were increased, the load capacity

Table 6
Ranges of the design variables.

	Load capacity (kN)		Ultimate deflection (mm)	
	Lower bound	Upper bound	Lower bound	Upper bound
H (mm)	260	300	250	300
W_1 (mm)	310	420	300	380
W_2 (mm)	300	400	300	390
T_1(mm)	45	65	40	60
T_2(mm)	30	40	28	40
T_3(mm)	30	50	30	45

and deflection first increased and then decreased, but they did not achieve the maximum values simultaneously. Table 6 lists the ranges of the design variables that are varied to achieve the best overall performance of the assemblages. The ranges are selected to include the values that achieve the highest load capacity and deflection while being reasonable for fabrication.

3.5. Prediction results

Sequential surrogate models were trained using the data obtained from the finite element model and used to predict the mechanical properties of the assemblages. For the training of the sequential surrogate models, first, initial datasets were generated using the finite element model for the training and validation of the sequential surrogate models, and then new samples were sequentially added to the training dataset to improve the accuracy of the sequential surrogate models until adequate accuracy is achieved. In this study, the initial dataset was formed using the results from 10 finite element models, and 60 finite element models were established to generate new samples to enrich the training dataset. Fig. 13 compares the prediction results with the actual results of the load capacity, ultimate deflection, and stiffness. The actual results were obtained from the finite element model, and the predicted results were obtained from the sequential surrogate model. The values of R^2 corresponding to validation and training datasets are higher than 0.94, indicating that the sequential surrogate models can reasonably predict the mechanical properties of the assemblages of the modular blocks.

The validation performance metrics of sequential surrogate models for predicting the load capacity, ultimate deflection, and stiffness were evaluated (Fig. A2 in Appendix). The results of R^2 and *RMSE* increase as more sample are added to the training dataset, meaning that the prediction accuracy of sequential surrogate models is improved by increasing the training dataset. The performance metrics converged to certain values after sufficient samples were added to the training dataset. Table 7 shows the results of the performance metrics of the training and validation datasets for predicting the mechanical properties of the assemblages. The values of R^2 are higher than 0.98 for the training dataset and higher than 0.94 for the validation dataset. The *RMSE* of the load capacity is only 0.04 kN for the training dataset and 0.91 kN for the validation dataset. In short, the trained sequential surrogate models provide reasonable prediction of the mechanical properties of the assemblages.

3.6. Many-objective optimization results

Table 8 lists four design objectives for many-objective optimization

Table 7
The performance metrics of the sequential surrogate modeling.

Dataset	Performance metric	Load capacity (kN)	Deflection (mm)	Stiffness (kN/mm)
Training	R^2	0.99	0.98	0.98
	RMSE	0.04	0.10	0.18
Validation	R^2	0.96	0.94	0.97
	RMSE	0.91	0.16	0.93

Table 8
Description of the design objectives.

Design objective	Description	Goal
F_1	Load capacity	Maximization
F_2	Ultimate deflection	Maximization
F_3	Stiffness	Maximization
F_4	Volume	Minimization

of the modular blocks. Three objective functions F_1, F_2, and F_3 are defined for mechanical properties such as the load capacity, ultimate deflection, and stiffness of the assemblage, in order to ensure the mechanical performance. One objective function F_4 is defined for the volume of the modular block, in order to reduce material consumption.

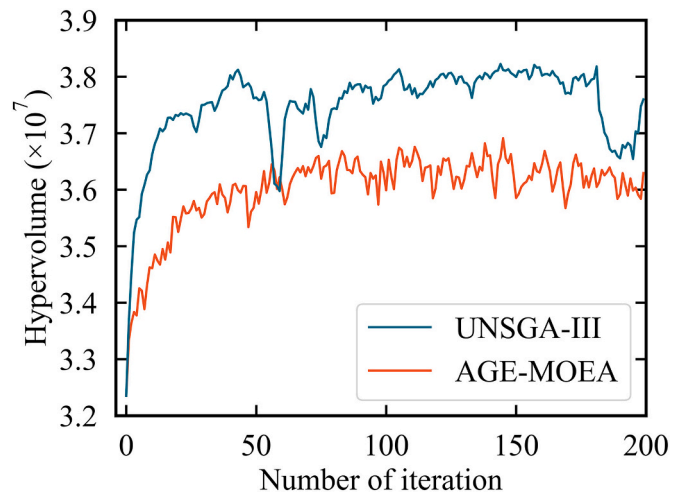The hypervolume indicators of UNSGA-III and AGEMOEA during

Fig. 14. Hypervolume indicator of the provided solutions for the best trials.
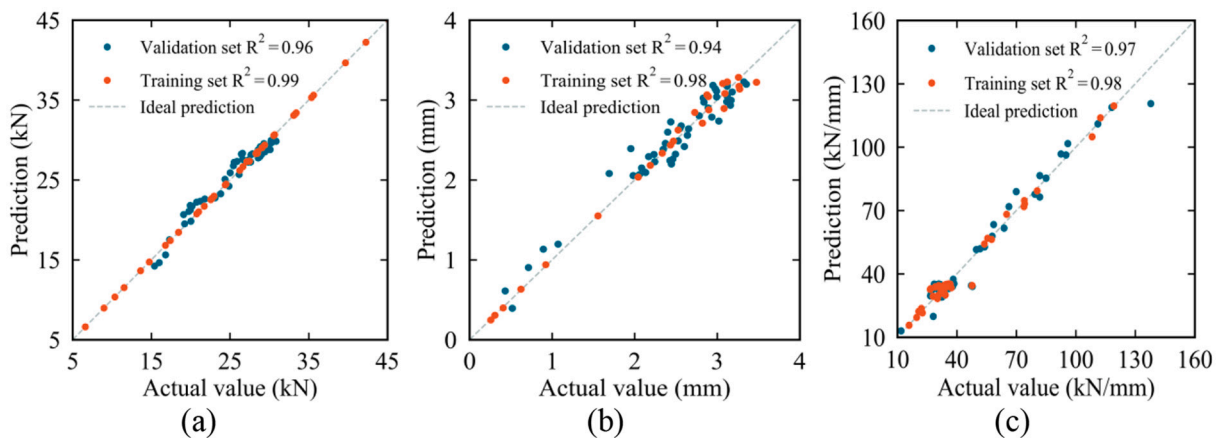

Fig. 13. Comparison of the predicted and actual results of (a) the load capacity, (b) the ultimate deflection corresponding to the peak load, and (c) the stiffness of the elastic stage.

optimization process are studied to compare the performance of methods. Fig. 14 shows the hypervolume results corresponding to maximizing load capacity, deflection, stiffness, and minimizing volume. The hypervolume indicator increases as the number of iterations increases, showing that the methods were able to iteratively improve the solutions. In each iteration, the magnitude of hypervolume indicator of UNSGA-III is greater than that of AGEMOEA. Therefore, UNSGA-III algorithm has better performance and is chosen for obtaining the optimal design variables of modular blocks.

Fig. 15 shows a set of the Pareto optimal solutions. There is a trade-off between the different objective functions. With the Pareto optimal solutions, it is impossible to improve one objective function without compromising the other objective functions. The different Pareto optimal solutions are ranked using the TOPSIS method. The top ten Pareto optimal solutions are shown in Table 9. The Pareto optimal solutions are ranked based on the distance between the Pareto optimal solutions and the ideal solutions. The Pareto optimal solutions with shorter distances to the ideal solution are ranked higher.

Table 10 compares the original design with the optimal design obtained by the ranking using the TOPSIS method. The design variables H, W_1, and W_2 of the optimal solution are in the ranges of design variables listed in Table 5. The load capacity, deflection, and stiffness of the optimal design are improved by 23%, 12%, and 129%, respectively, and the volume is reduced by 52%. The proposed design framework can be utilized when there are constraints for the sizes of individuals modules due to transport and manufacturing restrictions. For example, various blocks can be designed with preset H, W_1, and W_2, respectively, while the other variables are optimized to achieve the best performance.

The results of the different design scenarios are listed in Table 11. The results show that the largest load capacity is achieved when H, W_1, W_2, T_1, T_2, and T_3 are 300 mm, 312 mm, 250 mm, 44 mm, 23 mm, and 50 mm, respectively. The largest ultimate deflection is achieved when H, W_1, W_2, T_1, T_2, and T_3 are 200 mm, 389 mm, 250 mm, 61 mm, 31 mm, and 29 mm, respectively. The largest stiffness is achieved when H, W_1, W_2, T_1, T_2, and T_3 are 406 mm, 200 mm, 250 mm, 34 mm, 23 mm, and 50 mm, respectively. The smallest volume is achieved when H, W_1, W_2, T_1, T_2, and T_3 are 220 mm, 298 mm, 200 mm, 43 mm, 31 mm, and 32 mm, respectively.

Various optimal design solutions are obtained when different objective functions are considered in the optimization process, as shown in Fig. 16. The optimal design solution for the maximal load capacity, ultimate deflection, stiffness, and the minimal volume is shown in Fig. 16(a). The optimal design solutions for the individual properties are shown in Figs. 16(b) to 16(d). The optimal design solutions for the maximal ultimate deflection and stiffness have the largest W_2 and H, respectively.
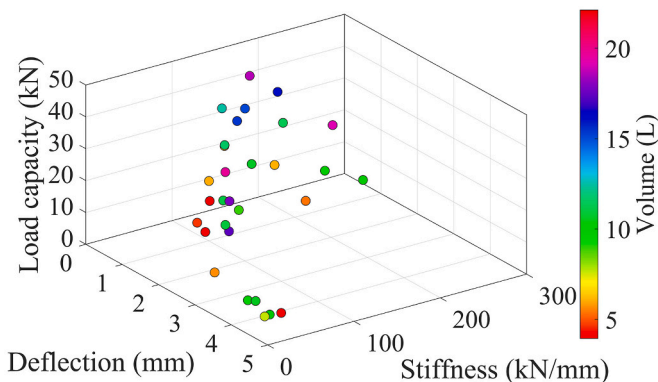
Table 9
Ranking of the Pareto optimal solutions using the TOPSIS method.

Rank	Load capacity (kN)	Deflection (mm)	Stiffness (kN/mm)	Volume (L)
1	24.8	2.9	25.9	4.7
2	26.67	3.35	20.54	10.97
3	23.27	2.25	64.09	11.10
4	42.10	1.74	102.24	15.40
5	33.17	1.48	98.66	11.61
6	30.76	3.13	34.52	17.81
7	19.36	3.41	5.21	5.64
8	21.69	1.14	144.32	10.66
9	21.19	3.12	34.53	17.33
10	33.51	2.42	59.80	19.76

Table 10
The optimal design solutions and experiment model.

	Original design	Optimal design	Discrepancy
H	220 mm	231 mm	5.0%
W_1	325 mm	216 mm	−33.5%
W_2	300 mm	275 mm	−8.3%
T_1	50 mm	30 mm	−40.0%
T_2	30 mm	18 mm	−40.0%
T_3	30 mm	18 mm	−40.0%
Load capacity	20.2 kN	24.8 kN	22.8%
Ultimate deflection	2.6 mm	2.9 mm	11.5%
Stiffness	11.3 kN/mm	25.9 kN/mm	129.2%
Volume	9.7 L	4.7 L	−51.6%

4. Conclusions

This paper presents a many-objective optimization method for the design of Lego-inspired modular blocks. A high-fidelity finite element analysis was performed to predict the structural behaviors of the modular blocks. Four objective functions were defined to maximize the load capacity, deflection at the peak load, and stiffness of the blocks and to minimize the volume. Lego-inspired structures are promising to play significant roles in the next-generation architecture. This research is relevant to the development and application of Lego-inspired structures in terms of performance optimization for structures categorized in reference [50]. Based on above investigations, the following conclusions are drawn:

- The designed block failed prior to failure in the joints, suggesting that the design of the joints is feasible for avoiding joint failure. Flexural failure occurs prior to shear failure, meaning that the flexural properties control the load capacity, deformation, and stiffness of assemblages using the blocks. Due to the use of ECC, the specimens carried higher mechanical loads after crack were generated. Multiple cracks were generated in the specimens under flexural or shear loading.
- The convergence R^2 values for predicting the load capacity, deflection at the peak load, and stiffness using the sequential surrogate models are 0.96, 0.97, and 0.94, respectively, as evaluated using the validation datasets. The convergence root mean squared errors for predicting the load capacity and deflection are 0.91 kN and 0.16 mm, respectively, as evaluated using the validation datasets.
- The optimal design of the modular blocks using the UNSGA-III algorithm indicates that the load capacity, deflection, and stiffness are 1.23, 1.12, 2.29 times greater, while the volume is reduced by 51.6% in comparison to the original design. The desired design solutions proved that the proposed predictive models and many-objective optimization method provide an effective solution for design optimization of Lego-inspired modular blocks.

Fig. 15. Illustration of the Pareto optimal solutions for the design optimization of the blocks.

Table 11

The optimal design solutions of preset variables.

|	Preset H			Preset W_1			Preset W_2		
H (mm)	200	300	400	406	285	417	220	284	332
W_1 (mm)	389	312	244	200	300	400	298	287	309
W_2 (mm)	250	250	379	250	270	250	200	300	400
T_1 (mm)	61	44	30	34	49	37	43	45	30
T_2 (mm)	31	23	18	23	27	20	31	29	18
T_3 (mm)	29	50	18	50	37	27	32	34	19
Load capacity (kN)	15.7	29.4	9.8	5.02	29.1	19.8	11.6	28.7	19.6
Deflection (mm)	2.9	1.3	1.0	0.2	1.8	0.6	1.7	2.2	2.4
Stiffness (kN/mm)	48.2	124.3	56.7	203.0	87.5	197.0	82.1	62.0	27.0
Volume (L)	8.9	11.2	10.0	9.4	10.3	10.6	6.1	10.7	10.3
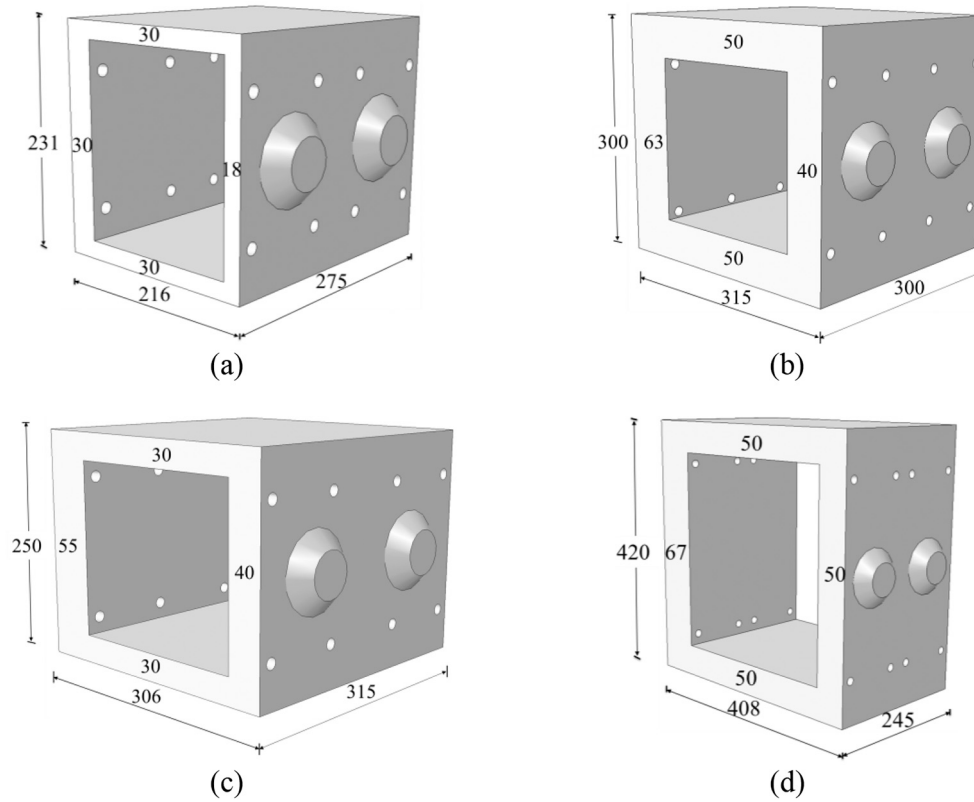
Fig. 16. The optimal solutions for: (a) the maximal load capacity, ultimate deflection, stiffness, and the minimal volume; (b) the maximal load capacity; (c) the maximal ultimate deflection; and (d) the maximal stiffness.

Declaration of Competing Interest

The authors declare that they have no known competing financial interests or personal relationships that could have appeared to influence the work reported in this paper.

Appendix

The appendix shows Figs. A1 and A2. Fig. A1 shows the effects of design variables of the blocks. Fig. A2 shows the convergence of performance metrics R^2 and *RMSE*.
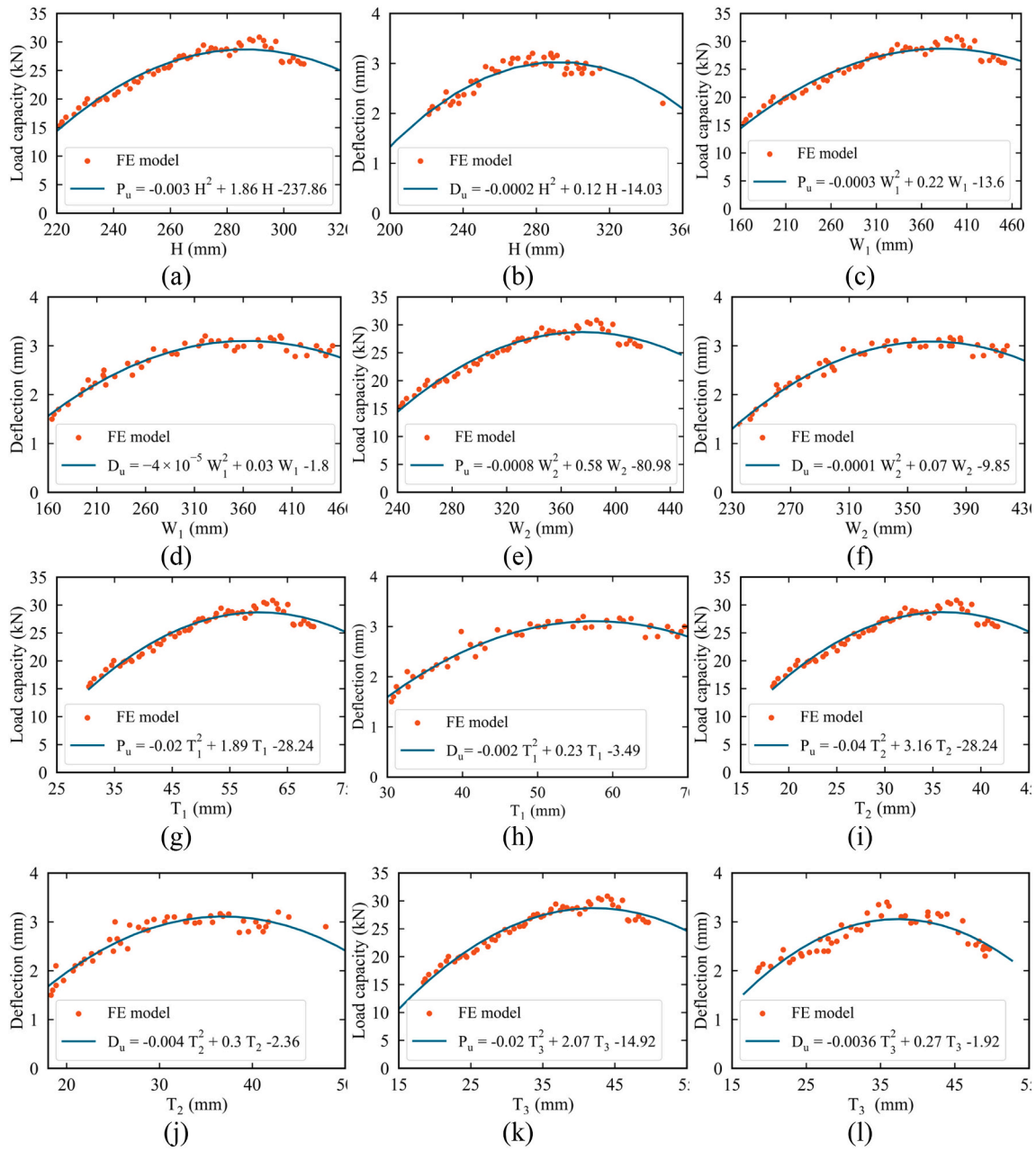
Fig. A1. Effects of H on: (a) the load capacity (P_u) and (b) ultimate deflection (D_u). Effects of W_1 on (c) P_u and (d) D_u. Effects of W_2 on (e) P_u and (f) D_u. Effects of T_1 on (g) P_u and (h) D_u. Effects of T_2 on (i) P_u and (j) deflection. Effects of T_3 on (k) P_u and (l) D_u.
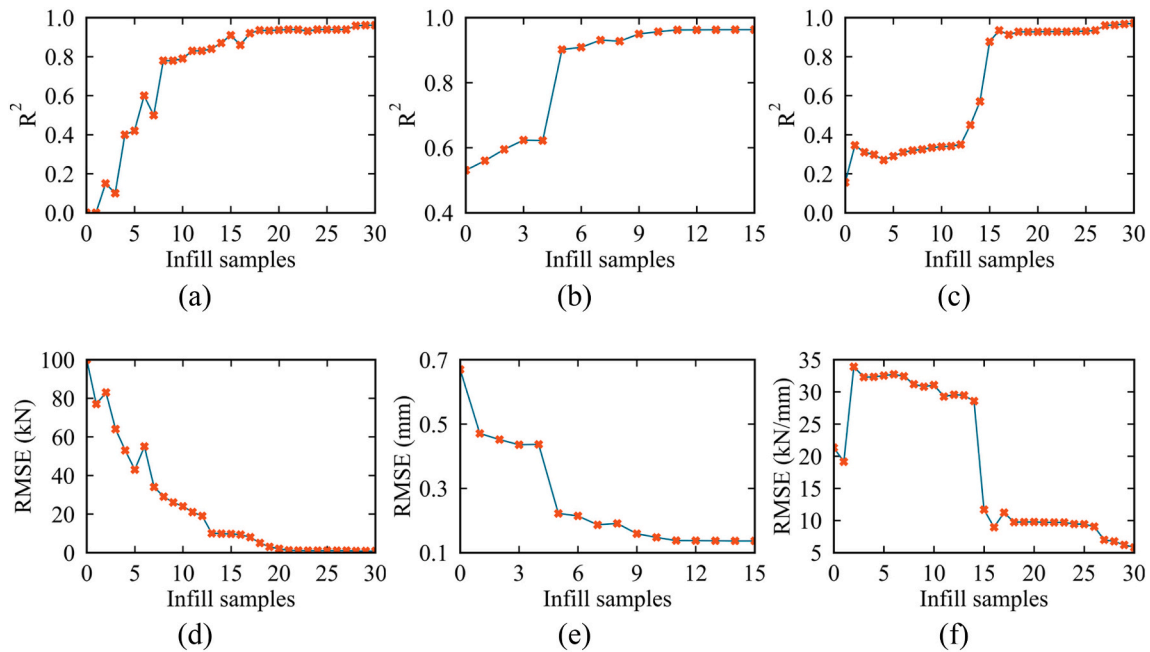
Fig. A2. Convergence results: (a) R^2 for load capacity; (b) R^2 for deflection; (c) R^2 for stiffness; (d) *RMSE* for load capacity; (e) *RMSE* for deflection; and (f) *RMSE* for stiffness.

References

[1] F. Barbosa, J. Woetzel, J. Mischke, M.J. Ribeirinho, M. Sridhar, M. Parsons, N. Bertram, S. Brown, Reinventing construction through a productivity revolution| McKinsey. https://www.mckinsey.com/industries/capital-projects-andinfrastructure/our-insights/reinventing-construction-through-a-productivity-revolution, 2017.

[2] R.Y. Zhong, X. Xu, E. Klotz, S.T. Newman, Intelligent manufacturing in the context of industry 4.0: a review, Engineering 3 (5) (2017) 616–630, https://doi.org/10.1016/J.ENG.2017.05.015.

[3] N. Bertram, S. Fuchs, J. Mischke, R. Palter, G. Strube, J. Woetzel, Modular construction: from projects to products, McKinsey & Company: Capital Projects & Infrastructure (2019) 1–34. https://www.ivvd.nl/wp-content/uploads/2019/12/Modular-construction-from-projects-to-products-full-report-NEW.pdf.

[4] M. Goh, Y.M. Goh, Lean production theory-based simulation of modular construction processes, Autom. Constr. 101 (2019) 227–244, https://doi.org/10.1016/j.autcon.2018.12.017.

[5] X. Li, G.Q. Shen, P. Wu, T. Yue, Integrating building information modeling and prefabrication housing production, Autom. Constr. 100 (2019) 46–60, https://doi.org/10.1016/j.autcon.2018.12.024.

[6] W. Ferdous, Y. Bai, T.D. Ngo, A. Manalo, P. Mendis, New advancements, challenges and opportunities of multi-storey modular buildings–a state-of-the-art review, Eng. Struct. 183 (2019) 883–893, https://doi.org/10.1016/j.engstruct.2019.01.061.

[7] M. Kamali, K. Hewage, Life cycle performance of modular buildings: a critical review, Renew. Sust. Energ. Rev. 62 (2016) 1171–1183, https://doi.org/10.1016/j.rser.2016.05.031.

[8] E. McCarthy, T. Wright, J.E. Padgett, R. DesRoches, P. Bradford, Development of an experimentally validated analytical model for modular bridge expansion joint behavior, J. Bridg. Eng. 19 (2) (2014) 235–244, https://doi.org/10.1061/(ASCE)BE.1943-5592.0000521.

[9] J. Qi, Y. Bao, J. Wang, L. Li, W. Li, Flexural behavior of an innovative dovetail UHPC joint in composite bridges under negative bending moment, Eng. Struct. 200 (2019), 109716, https://doi.org/10.1016/j.engstruct.2019.109716.

[10] A.W. Lacey, W. Chen, H. Hao, K. Bi, Effect of inter-module connection stiffness on structural response of a modular steel building subjected to wind and earthquake load, Eng. Struct. 213 (2020), 110628, https://doi.org/10.1016/j.engstruct.2020.110628.

[11] Z. Chen, Y. Liu, X. Zhong, J. Liu, Rotational stiffness of inter-module connection in mid-rise modular steel buildings, Eng. Struct. 196 (2019), 109273, https://doi.org/10.1016/j.engstruct.2019.06.009.

[12] S. Mor, K. Ravindra, R.P. Dahiya, A. Chandra, Leachate characterization and assessment of groundwater pollution near municipal solid waste landfill site, Environ. Monit. Assess. 118 (1) (2006) 435–456, https://doi.org/10.1007/s10661-006-1505-7.

[13] J.V. Puthussery, R. Kumar, A. Garg, Evaluation of recycled concrete aggregates for their suitability in construction activities: an experimental study, Waste Manag. 60 (2017) 270–276, https://doi.org/10.1016/j.wasman.2016.06.008.

[14] M. Casuccio, M.C. Torrijos, G. Giaccio, R. Zerbino, Failure mechanism of recycled aggregate concrete, Constr. Build. Mater. 22 (7) (2008) 1500–1506, https://doi.org/10.1016/j.conbuildmat.2007.03.032.

[15] C. Thomas, J. Setién, J. Polanco, P. Alaejos, M.S. De Juan, Durability of recycled aggregate concrete, Constr. Build. Mater. 40 (2013) 1054–1065, https://doi.org/10.1016/j.conbuildmat.2012.11.106.

[16] Y. Bao, V.C. Li, Feasibility study of Lego-inspired construction with bendable concrete, Autom. Constr. 113 (2020), 103161, https://doi.org/10.1016/j.autcon.2020.103161.

[17] M.D. Mckay, R.J. Beckman, W. Conover, A comparison of three methods for selecting values of input variables in the analysis of output from a computer code, Technometrics 42 (1) (2000) 55–61, https://doi.org/10.2307/1268522.

[18] S.-S. Jin, H.-J. Jung, Sequential surrogate modeling for efficient finite element model updating, Comput. Struct. 168 (2016) 30–45, https://doi.org/10.1016/j.compstruc.2016.02.005.

[19] S. Mahjoubi, R. Barhemat, P. Guo, W. Meng, Y. Bao, Prediction and multi-objective optimization of mechanical, economical, and environmental properties for strain-hardening cementitious composites (SHCC) based on automated machine learning and metaheuristic algorithms, J. Clean. Prod. 329 (2021) 129665, https://doi.org/10.1016/j.jclepro.2021.129665.

[20] C.-L. Hwang, K. Yoon, Methods for Multiple Attribute Decision Making, Multiple Attribute Decision Making, 1981, pp. 58–191, https://doi.org/10.1007/978-3-642-48318-9_3.

[21] R.L. Iman, J.C. Helton, J.E. Campbell, An approach to sensitivity analysis of computer models: part I—Introduction, input variable selection and preliminary variable assessment, J. Qual. Technol. 13 (3) (1981) 174–183, https://doi.org/10.1080/00224065.1981.11978748.

[22] J.L. Loeppky, J. Sacks, W.J. Welch, Choosing the sample size of a computer experiment: a practical guide, Technometrics 51 (4) (2009) 366–376, https://doi.org/10.1198/TECH.2009.08040.

[23] A. Garbo, B.J. German, Performance assessment of a cross-validation sampling strategy with active surrogate model selection, Struct. Multidiscip. Optim. 59 (6) (2019) 2257–2272, https://doi.org/10.1007/s00158-018-02190-7.

[24] J. Eason, S. Cremaschi, Adaptive sequential sampling for surrogate model generation with artificial neural networks, Comput. Chem. Eng. 68 (2014) 220–232, https://doi.org/10.1016/j.compchemeng.2014.05.021.

[25] J.L.O. Mark, Introduction to Radial Basis Function Networks. Technical Report, Center for Cognitive Science, University of Edinburgh, 1996. https://faculty.cc.gatech.edu/~isbell/tutorials/rbf-intro.pdf.

[26] J.P. Kleijnen, Kriging metamodeling in simulation: a review, Eur. J. Oper. Res. 192 (3) (2009) 707–716, https://doi.org/10.1016/j.ejor.2007.10.013.

[27] S.C. Wang, Artificial Neural Network. Interdisciplinary Computing in Java Programming, 2003, pp. 81–100, https://doi.org/10.1007/978-1-4615-0377-4_5.

[28] Y. Zhao, W. Lu, C. Xiao, A kriging surrogate model coupled in simulation–optimization approach for identifying release history of groundwater sources, J. Contam. Hydrol. 185 (2016) 51–60, https://doi.org/10.1016/j.jconhyd.2016.01.004.

[29] D.G. Krige, A statistical approach to some basic mine valuation problems on the Witwatersrand, J. South. Afr. Inst. Min. Metall. 52 (6) (1951) 119–139. https://hdl.handle.net/10520/AJA0038223X_4792.

[30] A. Panichella, An adaptive evolutionary algorithm based on non-Euclidean geometry for many-objective optimization, in: Proceedings of the Genetic and Evolutionary Computation Conference, 2019, pp. 595–603, https://doi.org/10.1145/3321707.3321839.

[31] Construction Robotics. https://www.construction-robotics.com/. Accessed on October 1, 2021.

[32] S. Mahjoubi, R. Barhemat, Y. Bao, Optimal placement of triaxial accelerometers using hypotrochoid spiral optimization algorithm for automated monitoring of high-rise buildings, Autom. Constr. 118 (2020), 103273, https://doi.org/10.1016/j.autcon.2020.103273.

[33] V.C. Li, C.K. Leung, Steady-state and multiple cracking of short random fiber composites, J. Eng. Mech. 118 (11) (1992) 2246–2264, https://doi.org/10.1061/(ASCE)0733-9399(1992)118:11(2246).

[34] V.C. Li, On engineered cementitious composites (ECC) a review of the material and its applications, J. Adv. Concr. Technol. 1 (3) (2003) 215–230, https://doi.org/10.3151/jact.1.215.

[35] X. Li, X. Lv, X. Zhou, W. Meng, Y. Bao, Upcycling of waste concrete in eco-friendly strain-hardening cementitious composites: mixture design, structural performance, and life-cycle assessment, J. Clean. Prod. 330 (2022), 129911, https://doi.org/10.1016/j.jclepro.2021.129911.

[36] T. Kanda, V.C. Li, Practical design criteria for saturated pseudo strain hardening behavior in ECC, J. Adv. Concr. Technol. 4 (1) (2006) 59–72, https://doi.org/10.3151/jact.4.59.

[37] X. Li, Y. Li, M. Yan, W. Meng, X. Lu, K. Chen, Y. Bao, Cyclic behavior of joints assembled using prefabricated beams and columns with engineered cementitious composite, Eng. Struct. 247 (2021) 113115, https://doi.org/10.1016/j.engstruct.2021.113115.

[38] X. Li, J. Wang, Y. Bao, G. Chen, Cyclic behavior of damaged reinforced concrete columns repaired with high-performance fiber-reinforced cementitious composite, Eng. Struct. 136 (2017) 26–35, https://doi.org/10.1016/j.engstruct.2017.01.015.

[39] X. Li, Z. Xu, Y. Bao, Z. Cong, Post-fire seismic behavior of two-bay two-story frames with high-performance fiber-reinforced cementitious composite joints, Eng. Struct. 183 (2019) 150–159, https://doi.org/10.1016/j.engstruct.2019.01.015.

[40] E.H. Yang, V.C. Li, Tailoring engineered cementitious composites for impact resistance, Cem. Concr. Res. 42 (8) (2012) 1066–1071, https://doi.org/10.1016/j.cemconres.2012.04.006.

[41] S. Qian, M.D. Lepech, V.C. Li, Elevating ECC material ductility to structural performance of steel anchoring to concrete. International RILEM workshop on high performance Fiber reinforced cementitious composites (HPFRCC), in: Structural Applications, Honolulu, Hawaii, May 23–26, 2005, 2006. https://deepblue.lib.umich.edu/bitstream/handle/2027.42/84788/elevating_QianAndLi2005.pdf?sequence=1.

[42] X. Li, Y. Bao, L. Wu, Q. Yan, H. Ma, G. Chen, H. Zhang, Thermal and mechanical properties of high-performance fiber-reinforced cementitious composites after exposure to high temperatures, Constr. Build. Mater. 157 (2017) 829–838, https://doi.org/10.1016/j.conbuildmat.2017.09.125.

[43] V.C. Li, High-performance and multifunctional cement-based composite material, Engineering 5 (2) (2019) 250–260, https://doi.org/10.1016/j.eng.2018.11.031.

[44] Y. Yang, M.D. Lepech, E.H. Yang, V.C. Li, Autogenous healing of engineered cementitious composites under wet–dry cycles, Cem. Concr. Res. 39 (5) (2009) 382–390, https://doi.org/10.1016/j.cemconres.2009.01.013.

[45] X. Li, Y. Bao, N. Xue, G. Chen, Bond strength of steel bars embedded in high-performance fiber-reinforced cementitious composite before and after exposure to elevated temperatures, Fire Saf. J. 92 (2017) 98–106, https://doi.org/10.1016/j.firesaf.2017.06.006.

[46] M. Xu, H. Clack, T. Xia, Y. Bao, K. Wu, H. Shi, V. Li, Effect of TiO2 and fly ash on photocatalytic NOx abatement of engineered cementitious composites, Constr. Build. Mater. 236 (2020), 117559, https://doi.org/10.1016/j.conbuildmat.2019.117559.

[47] M. Şahmaran, V.C. Li, Durability properties of micro-cracked ECC containing high volumes fly ash, Cem. Concr. Res. 39 (11) (2009) 1033–1043, https://doi.org/10.1016/j.cemconres.2009.07.009.

[48] ASTM C109 / C109M - 20b, Standard Test Method for Compressive Strength of Hydraulic Cement Mortars (using 2-in. or [50-mm] Cube Specimens), ASTM International, United States, 2020. https://www.astm.org/c0109_c0109m-20.html.

[49] JSCE, Recommendations for Design and Construction of High Performance fiber Reinforced Cement Composites with Multiple Fine Cracks, Japan Society of Civil Engineers, Tokyo, Japan, 2008. https://www.jsce.or.jp/committee/concrete/e/hpfrcc_JSCE.pdf.

[50] B. Ekici, C. Cubukcuoglu, M. Turrin, I.S. Sariyildiz, Performative computational architecture using swarm and evolutionary optimisation: a review, Build. Environ. 147 (2019) 356–371, https://doi.org/10.1016/j.buildenv.2018.10.023.